

RESEARCH

Open Access



Tumor microenvironment-responsive precise delivery nanocarrier potentiating synchronous radionuclide therapy and chemotherapy against cancer

Jie An^{1,2,3†}, Qin Zhou^{1,2,3,4†}, Kaile Chu^{1,2,3,4}, Siyuan Chen^{1,2,3}, Chenliang Niu⁴, Weiming Zhang^{1,2,3,4}, Jie Gao⁵, Min Li^{1,2,3}, Jianbo Cao^{1,2,3}, Junping Lv^{1,2,3}, Di Zhang^{1,2,3}, Zhifang Wu^{1,2,3}, Sijin Li^{1,2,3*} and Hua Wei^{1,2,3*}

Abstract

To achieve better therapeutic outcomes in cancer treatment, the combination of radionuclide and chemotherapy is commonly employed in clinical practice. However, the primary challenge lies in achieving precise drug delivery to tumor tissues, often leading to suboptimal therapeutic efficacy. This study presents a novel, tumor microenvironment-responsive drug delivery carrier that integrates real-time MRI/SPECT dual-modal imaging for precise diagnosis and treatment monitoring. The carrier comprised is based on a hybrid structure composed of hyaluronic acid (HA) and human serum albumin (HSA), encapsulating the metal-organic framework MIL-100(Fe). It was loaded with the chemotherapeutic drug doxorubicin (DOX) and modified with the radionuclide ¹³¹I, designed to precise diagnosis and treatment of tumors. HA binds specifically to the overexpressed CD44 receptor on the tumor surface, ensuring that the carrier targets tumors selectively. The incorporated ¹³¹I emits β rays, which deliver ionizing radiation to eradicate tumor cells. Concurrently, the carrier could release DOX in response to the tumor microenvironment, inhibiting DNA synthesis and sensitizing the tumor cells to radiation. This combined approach results in synchronous radionuclide therapy (RNT) and chemotherapy, maximizing therapeutic impact. In vitro and in vivo experiments demonstrated that the carrier exhibited favorable biocompatibility, stable radionuclide labeling, tumor-specific accumulation, and controlled release of DOX within the tumor microenvironment. Furthermore, MRI/SPECT dual-modal imaging enabled real-time tumor localization and monitoring of the carrier in vivo biodistribution. Experimental outcomes confirmed that this innovative carrier, combining RNT and chemotherapy, significantly inhibited tumor growth. This strategy offers a promising approach for precision radio-chemotherapy guided by dual-modal imaging, providing valuable insights for integrated targeted diagnosis and treatment of tumors.

[†]Jie An and Qin Zhou contributed equally to this work.

*Correspondence:

Sijin Li

lisjnm123@163.com

Hua Wei

jennyhua1981@sina.com

Full list of author information is available at the end of the article



Keywords Radionuclide therapy, Chemotherapy, SPECT/MRI, Tumor microenvironment-responsive

Introduction

Combination therapies involving radionuclide and chemotherapy are commonly employed to improve cancer treatment outcomes. However, the systemic administration of radionuclide and anticancer drugs frequently results in rapid metabolism and nonspecific distribution, leading to significant toxic effects on patients [1, 2]. To mitigate these issues, nanomedicine strategies have been developed to improve radionuclide delivery efficiency, enhance lesion detection sensitivity, and boost tumor treatment efficacy [3–5]. Nanocarriers, owing to their unique physical, chemical, and biological properties, can co-deliver multiple drugs or imaging agents [6]. By designing nanocarriers that integrate both therapeutic and diagnostic functions, they enable imaging-guided control of drug release and targeted therapy [7]. This approach increases local drug concentration and enables precise treatment. Radionuclide-labeled nanocarriers offer an effective approach to overcome challenges in cancer diagnosis and treatment.

Radionuclide therapy eradicates tumor cells by emitting α or β rays, but its efficacy is often limited by insufficient radiation deposition, necessitating frequent high-dose radiation. This can lead to severe side effects such as immunosuppression and hematopoietic defects [8, 9]. Therefore, ensuring the targeted delivery of an adequate dose of radionuclide to tumor tissues is crucial for the success of radionuclide therapy. Numerous studies have shown that surface functionalization of nanocarriers with ligands specific to tumors for active targeting increases their aggregation in tumor locations [10–12]. Hyaluronic acid (HA), a natural polysaccharide, plays a key role in tumorigenesis and has a strong affinity for the CD44 receptor, which is overexpressed on various cancer cells and cancer stem cells [13]. Thus, it's widely utilized for active tumor-targeted delivery of drugs and genes. However, the therapeutic efficacy of radionuclide therapy can be weakened over time, potentially leading to radiation resistance in tumor cells. In clinical practice, combining radiotherapy with chemotherapy is common, as chemotherapy drugs can enhance the sensitivity of radiation, increasing the anti-tumor effect [14, 15]. However, separate administering of radiotherapy and chemotherapy may result in inconsistent pharmacokinetics and tumor homing curves, hindering to achieve optimal treatment outcome [16]. Utilizing nanocarriers to co-deliver radionuclides and chemotherapeutic agents offers a promising solution, improving therapeutic efficacy while minimizing the adverse effects typically associated with radionuclide therapy.

Exploring new strategies for precise and effective delivery of sufficient therapeutic agents to tumor sites has attracted considerable attention [17]. One key challenge in nanocarrier-based systems is the leakage of drugs during transport. Precise control of drug release is an effective approach to overcome this issue. Researchers have proposed various stimuli-responsive designs that target unique features of the tumor microenvironment, such as pH, redox state, reactive oxygen species, etc., to achieve controlled drug release [18–20]. The tumor microenvironment is characterized by a weakly acidic pH (pH = 5.5–6.5) due to the extensive anaerobic glycolysis in tumor cells, which is lower than that of normal tissues. Additionally, the high concentration and reducing nature of glutathione (GSH) in tumor cells create environment, serving as a target for controlled drug release [21]. Therefore, the weakly acidic and high GSH microenvironment of tumor sites can be utilized to control drug release without relying on external stimuli, significantly improving the bioavailability of therapeutic agents through dual-stimuli responsiveness. Consequently, the development of nanocarriers with targeting capabilities and tumor microenvironment-responsive properties is a promising strategy for enhancing the therapeutic efficacy of drugs.

Metal-organic frameworks (MOFs), a novel self-assembled porous material with metal connectors and organic bridging ligands, have been extensively studied and applied in various potential biomedical fields [22]. Among them, iron-based MOFs, such as MIL-100(Fe), are notable for attention due to their high porosity, large surface area, biocompatibility, and biodegradability. They can serve as carriers for drug delivery and as T_2 contrast agents for magnetic resonance imaging (MRI) [23, 24]. Human serum albumin (HSA), a naturally abundant serum protein in the human body, possesses inherent biocompatibility and has been widely recognized as an optimal drug carrier for chemotherapeutic agents, photosensitizers, and radionuclide. The tyrosine-rich surface of HSA also provides functional groups for specific labeling with radionuclide [25, 26].

In this study, an intelligent delivery system was designed by combining HA and HSA to encapsulate MIL-100(Fe), while simultaneously loading the chemotherapeutic drug doxorubicin (DOX) and the radionuclide ^{131}I . This system enables real-time monitoring of combined radionuclide therapy and chemotherapy with magnetic resonance imaging (MRI) and single-photon emission computed tomography (SPECT) dual-model imaging (Fig. 1). The carrier utilized HSA and MIL-100(Fe) to load DOX, while the abundant tyrosine on the surface of HSA provides effective binding sites for

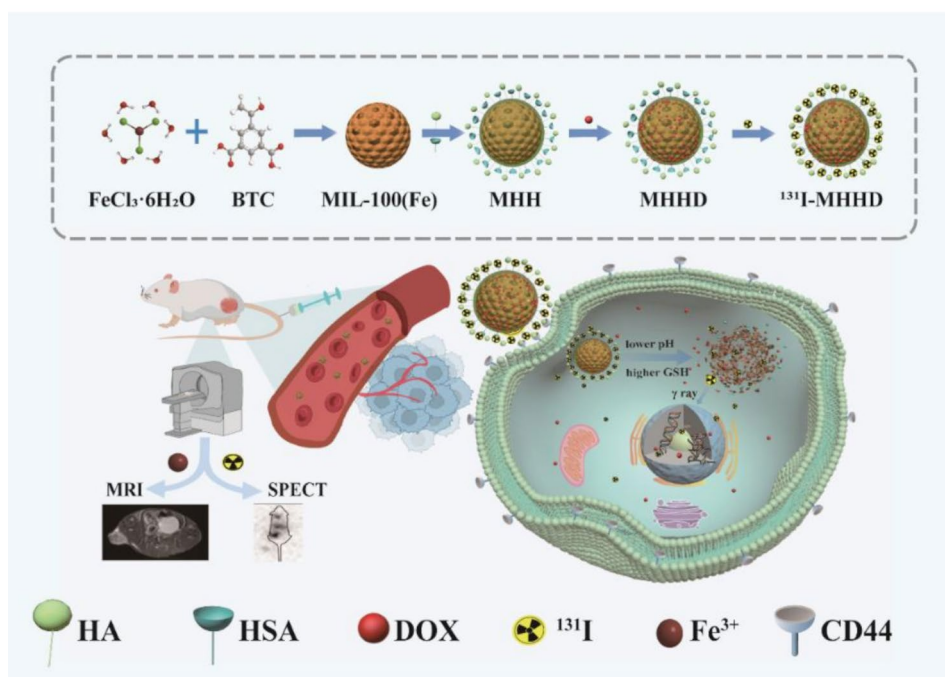


Fig. 1 Schematic illustration of the synthesis route of ^{131}I -MHHD and MRI/SPECT imaging guided synchronous radionuclide and chemotherapy against tumor

the labeling of ^{131}I [27]. This allows for the precise delivery of both radioactive isotopes and chemotherapeutic agents specifically to tumor cells with overexpressed the CD44 receptor using the targeting capabilities of HA [28]. Furthermore, the carrier exhibits tumor microenvironment-responsive properties, enabling controlled drug release upon encountering the unique conditions at the tumor site, thereby minimizing its toxic side effects. This system enhances the therapeutic effect by combining radionuclide therapy and chemotherapy for a synchronized, synergistic treatment of tumors. In addition to its dual-modal imaging capabilities via MRI and SPECT, the carrier also enables real-time monitoring of drug distribution in vivo and supports tumor diagnosis. This radionuclide-labeled carrier provides a new approach for the diagnosis and against of tumors.

Materials and methods

Materials

1,3,5-benzenetricarboxylic acid (trimesic acid, BTC), iron trichloride hexahydrate ($\text{FeCl}_3 \cdot 6\text{H}_2\text{O}$), doxorubicin hydrochloride, hyaluronic acid, and chloramine T trihydrate were purchased from Shanghai Aladdin Biochemical Technology Co., Ltd. Methanol, anhydrous ethanol were purchased from Tianjin Fangdatong Zheng Chemical Co., Ltd. Na^{131}I were provided by the Department of Nuclear Medicine. DMEM medium, fetal bovine serum (FBS), penicillin-streptomycin solution and trypsin sourced from Gibco. All the reagents used in the

experiment were of analytical grade and used without further purification. 4T1 mouse breast cancer cells were purchased from Procell Life Science&Technology Co., Ltd. Balb/C mice (female, 4-weeks-old) were acquired from SPF (Beijing) Biotechnology Co., Ltd. MRI was performed using 7.0T Micro MRI machine (Bruker, Germany).

Characterizations

The morphology of MII-100(Fe) and MHHD was observed by HT7700 transmission electron microscope (Hitachi, Japan). The size and potential of MIL-100(Fe) and MHHD were measured by Zetasizer Labblue (Malvern, the United Kingdom). The UV Visible absorption spectrum was performed by UH 5700 UV-Vis Spectrophotometer (Hitachi, Japan). Elemental analysis of MII-100(Fe) was performed using ESCALAB 250XI X-ray photoelectron spectroscopy (Thermo, the United States).

Synthesis of MII-100(Fe)

First, 7.5 mM solution of $\text{FeCl}_3 \cdot 6\text{H}_2\text{O}$ (in methanol) was prepared and mixed with 7.5 mM solution of BTC solution in 40 mL of methanol. The mixture was vigorously stirred for about 10 min at room temperature. Afterward, the resulting solution was transferred into a 70 °C oil-bath and reacted for 90 min. The reaction product was collected by centrifugation and washed 3 times with ethanol and deionized water. Finally, the freeze-dried product was stored at 4 °C for future use.

Synthesis of MHH, MHD, MHHD nanoprobe

MIL-100(Fe) was mixed with HSA at a weight ratio of 5:1, or with HA and HSA at a weight ratio of 10:1:1. The mixtures were stirred in an aqueous solution for 24 h to facilitate the co-assembly of MIL-100(Fe) with HSA (resulting in MIL-100(Fe)@HSA, denoted as MH) or with HA/HSA (resulting in MIL-100(Fe)@HA-HSA, denoted as MHH). Subsequently, The MIL-100(Fe)@HSA@DOX (MHD) or MIL-100(Fe)@HA-HSA@DOX (MHHD) were obtained by mixing DOX with MH or MHH at weight ratio of 1:1 in aqueous solutions, followed by about 24 h of shaking in the dark.

Synthesis and stability of ^{131}I -MHH, ^{131}I -MHD, ^{131}I -MHHD

Na^{131}I (2 mCi), MHH (2 mg/mL, 1 mL) and chloramine T solution (10 mg/mL, 400 μL) were added in a 25 mL round-bottom flask. The mixture was stirred for 15 min at room temperature, after which the unlabeled ^{131}I was removed by centrifugation (10000 rpm, 10 min) to yield ^{131}I -MHH. The same method was followed to obtain ^{131}I -MHD and ^{131}I -MHHD.

To investigate whether ^{131}I in ^{131}I -MHH, ^{131}I -MHD, and ^{131}I -MHHD is stably covalently bound to the tyrosine residues of HSA rather than merely adsorbed on the surface, the following experimental procedure was conducted. Immediately after the reaction, the precipitates of ^{131}I -MHH, ^{131}I -MHD, and ^{131}I -MHHD were subjected to radioactivity measurement, denoted as CPM_0 . The precipitate was then resuspended in ultrapure water, sonicated for 1 min to ensure homogeneity, and centrifuged at 12,000 rpm for 10 min. The supernatant was carefully collected, and the radioactivity of free ^{131}I was measured and recorded as CPM_1 . The precipitate was subjected to six cycles of washing and centrifugation. The percentage of free ^{131}I in the supernatant was calculated using the formula: $(\text{CPM}_1/\text{CPM}_0) \times 100\%$.

To assess the labeling stability of ^{131}I -MHHD and ^{131}I -MHD in PBS (Control) and DMEM + 10% FBS (simulated tumor microenvironment), 40 μCi of ^{131}I -MHHD solutions mixing with 2 mL different pH (5.5/7.4) of PBS or DMEM + 10% FBS, respectively, and incubated at 37 °C. The stability was evaluated at various time points: 0, 0.5, 1, 2, 4, 6, 24, 48, 96, and 168 h. Before detection, thorough mixing with a pipette and sonicating for 1 min. The initial CPM value was recorded using a gamma counter. After centrifugation (12,000 rpm, 5 min), removed the supernatant to eliminate free ^{131}I the radioactivity of the precipitate was recorded as CPM_1 , while the radioactivity of solutions was recorded as CPM_0 before centrifugation. The ratio $\text{CPM}_1/\text{CPM}_0$ indicates the radiation stability of the reaction. Each experiment was conducted in triplicate. The radionuclide stabilization efficiency was calculated using the formula: $\text{radiation stabilization efficiency} = \text{CPM}_1/\text{CPM}_0 \times 100\%$.

The encapsulation efficiency and drug loading efficiency of DOX

The encapsulation efficiency and drug loading efficiency of DOX were analyzed and determined by UV visible spectrophotometer. Firstly, DOX was loaded into MH or MHH at a weight ratio of 1:1 to form MHD or MHHD, respectively. Subsequently, the resulting product was washed and centrifuged (12000 rpm, 10 min) with ultrapure water to remove unloaded free DOX until the supernatant became clear. The supernatant was collected, and the absorbance at wavelength of 480 nm was measured using the UV-visible spectrophotometer. The encapsulation efficiency (EE) and drug loading capacity (DLC) were calculated based on the following formulas:

$$\text{EE} (\%) = \frac{\text{weight of encapsulated DOX}}{\text{total weight of input DOX}} \times 100;$$

$$\text{DLC} (\%) = \frac{\text{weight of encapsulated DOX}}{\text{total weight of nanocarrier containing DOX}} \times 100;$$

Detecting the release rate of DOX in MHHD

To investigate the release rate of MHHD at different pH values, 2 mL of MHHD solution (with a DOX concentration of 0.4 mg/mL) was transferred into a dialysis bag (MWCO = 3500 Da). The dialysis bag was then placed in separate 10 mL PBS solutions with different pH values: pH 7.4, pH 5.5, pH 5.5 + 2 mM GSH and pH 5.5 + 10 mM GSH. The absorbance of DOX at 480 nm in the PBS solution was measured at various time intervals (0, 1, 2, 4, 6, 10, 24, 48, 72 h), and the percentage of DOX release was calculated.

Detecting the nuclear magnetic resonance (NMR) effect of MHHD

To verify the NMR effect of iron ions in MHHD, MRI was performed under different Fe^{3+} concentrations ($C_{\text{Fe}^{3+}} = 0, 0.1, 0.2, 0.4, 0.8 \text{ mM}$), and the relaxation rate R_2 ($1/T_2$) was calculated based on the relaxation time (T_2).

Hemolysis test and cytotoxicity assay

Whole blood was collected from healthy Balb/C mice and centrifuged (1500 r/min, 10 min) to obtain erythrocytes, which were then diluted with PBS. Subsequently, MHHD at varying concentrations (50, 100, 200, 400, 800 $\mu\text{g}/\text{mL}$) were diluted with 800 μL of PBS solution and incubated with 200 μL of diluted erythrocyte solution at 37 °C for 12 h. PBS and ultrapure water were used as positive and negative controls, respectively. After incubation, the tubes were then centrifuged (1500 r/min, 5 min) and the OD value of the supernatant was determined at 540 nm using a microplate reader. The hemolysis rate (HR) was calculated using the formula: $\text{HR} = (\text{OD}_{\text{sample}} - \text{OD}_{\text{negative control}}) / (\text{OD}_{\text{positive control}} - \text{OD}_{\text{negative control}}) \times 100\%$.

The cytotoxicity of MHH was determined using 4T1 mouse breast cancer cells. The 4T1 cells were inoculated in 96-well plates and incubated for 24 h. Following this, the cells were incubated with different concentrations of MHH (50, 100, 200, 400, 800 $\mu\text{g}/\text{mL}$). Then the original culture medium was removed, and 90 μL of DMEM culture medium along with 10 μL of CCK8 reagent were added to each well. After incubating for 2 h, the absorbance at 450 nm was measured by a microplate reader, and the cell survival rate was calculated. The cell survival rate = $(\text{OD}_{\text{sample}} - \text{OD}_{\text{blank}}) / (\text{OD}_{\text{control}} - \text{OD}_{\text{blank}}) \times 100\%$.

In vitro cellular uptake

NIH 3T3 and 4T1 cells were seeded in 6-well plate at a density of 2×10^6 cells per well and incubated for 24 h at 37 °C in 5% CO_2 . Once the cells that were grown to 90% confluency, they were treated with 1 mL MHHD (4.54 $\mu\text{g}/\text{mL}$, DOX at 2 μg), while untreated cells served as a negative control. After incubation of 1, 2, and 4 h, the cells were washed three times with PBS and harvested after trypsin digestion. The uptake of MHHD was quantified using a flow cytometer.

To further demonstrate the targeting, NIH 3T3 and 4T1 cells were seeded into laser confocal culture dishes and cultured overnight in the incubator at 37 °C in 5% CO_2 overnight. The next day, microscopic observation and cell counting were performed to ensure that the two cell types were approximately equal in number and both reached a confluence of 60%. Then 1 mL of MHHD (4.54 $\mu\text{g}/\text{mL}$, DOX at 2 μg) was added to the culture dish was incubated with 3T3/4T1 cells for 1, 2 and 4 h. The supernatant was then aspirated, and the cells were washed three times with PBS. The cell nucleus were stained with 100 μL of DAPI (1 $\mu\text{g}/\text{mL}$) for 10 min, followed by three additional washes. Finally, the uptake of DOX in cells was observed using a laser confocal microscope imaging instrument.

4T1 cells were separately seeded into 24-well plate and cultured overnight. Once the cells reached 80% confluency, they were treated with 1 mL of ^{131}I , ^{131}I -MHD, ^{131}I -MHHD (10 $\mu\text{Ci}/\text{mL}$) was added to the cells. The cells were then incubated for 5, 15, and 30 min, as well as 1, 3, 6, 12, and 24 h. After incubation, the culture medium was discarded, and the cells were washed three times with PBS. The radioactivity of each well was measured using a γ counter, recording the radioactive activity as CPM_1 . Blank control groups consisting of ^{131}I , ^{131}I -MHD, and ^{131}I -MHHD that were not co-cultured with cells were included in the experiment, with their radioactivity recorded as CPM_0 . Each experiment was performed in triplicate, and the calculation formula is: radioactive nuclide uptake rate = $\text{CPM}_1 / \text{CPM}_0 \times 100\%$.

In vitro therapeutic effect

NIH 3T3 and 4T1 cells were separately seeded into 96-well plate and cultured overnight. Then 100 μL of DMEM culture media with PBS, ^{131}I , ^{131}I -MHH, ^{131}I -MHD, MHHD, ^{131}I -MHHD (^{131}I at 3 μCi ; DOX at 2 μg) were added respectively. After incubation for 4 h, the cell survival rate was calculated.

4T1 cells were separately seeded into 24-well plate and cultured overnight. The culture medium was aspirated, and the cells were washed with PBS. Then, 1 mL of DMEM culture medium was added to each well. The experimental group was treated with ^{131}I and ^{131}I -MHH (^{131}I : 25 μCi), while the control group received no treatment. After 24 h of incubation, the cells were washed three times with PBS, digested with trypsin, and the digestion was terminated by adding DMEM. The cells were collected into EP tubes and centrifuged at 1000 rpm for 5 min. Following centrifugation, the cells were washed with PBS, and the supernatant was discarded. The cells were then resuspended in 195 μL of Annexin V-FITC binding solution, followed by the addition of 5 μL of Annexin V-FITC, gently mixed, and then 10 μL of propidium iodide (PI) was added and mixed thoroughly. After incubating at room temperature for 15 min, the samples were analyzed using a flow cytometer. In a parallel experiment, cells were treated as described for 24 h, and each well received Calcein AM and PI staining solution. After incubating at 37 °C in the dark for 20 min, the staining was observed under a fluorescence microscope.

4T1 cells were separately seeded into 12-well plate and cultured overnight. Then the cells were treated with PBS, ^{131}I , DOX, ^{131}I -MHH, ^{131}I -MHD, MHHD and ^{131}I -MHHD (DOX at 10 μg ; ^{131}I at 15 μCi) at different pH values (pH = 5.5 and 7.4), respectively. After incubation for 4 h, the cells were treated with γ -H2AX and DAPI and observed by fluorescence microscopy.

Dual modal SPECT/MRI

The tumor model (female, Balb/C, 4 weeks) was established by subcutaneous injection of 2×10^6 4T1 cells into the right hind limb of each mouse. When the tumor volume reached 200 mm^3 , mice were randomly divided into 3 groups and injected with MHHD (DOX = 1 mg/kg) through the tail vein or intratumoral injection. In vivo MRI was performed at various time points (0, 3, 6, 9, 12, 24 h and 3 d, 7 d) after injection using a 7.0T Micro MRI machine at room temperature, and the relaxation time (T_2) of the tumor site was recorded. T_2 -weighted MRI were acquired using the following parameters: repetition time (TR) = 2200, echo time (TE) = 8.0 ms, field of view (FOV) = 3.5 \times 3.5 mm, slice thickness = 1 mm, and 7 consecutive slices. The relaxation $R_2 = 1/T_2$ was calculated based on the relaxation time (T_2) of the mouse tumor site.

Similarly, the 4T1 tumor bearing mice were randomly divided into 3 groups and injected with 100 $\mu\text{L}^{131}\text{I}$ (200 μCi), ^{131}I -MHD (200 μCi) or ^{131}I -MHHD (200 μCi) through the tail vein or intratumoral injection. Whole body images of mice were obtained at different time points (0, 3, 6, 9, 12 and 24 h) after injection using ImaginE NET 632 SPECT system.

In vivo biodistribution evaluation

To quantify the biological distribution of ^{131}I -MHD in different organs, mice were injected with free ^{131}I and ^{131}I -MHHD through the tail vein. At different time points (0, 3, 6, 9, 12, 24 h), the mice were dissected, and organs including hearts, livers, spleens, lungs, kidneys, and tumors were collected. After weighing each organ, the radioactivity was measured using a gamma counter.

In vivo therapeutic effect evaluation and safety evaluation

When the tumor volume reached 100 mm^3 , tumor bearing mouse were randomly divided into five groups and injected with a total of 100 μL of PBS, ^{131}I (200 μCi), DOX, ^{131}I -MHD, MHHD and ^{131}I -MHD (DOX at 1 mg/kg, ^{131}I at 200 μCi) through the tail vein. The changes of weight in mice were recorded every other day. Tumor size was measured bi-daily using a vernier caliper, and tumor volume was calculated using the formula: tumor volume (mm^3) = $\frac{\text{Length} \times \text{Width}^2}{2}$. After 30 days, blood samples were collected from two groups of mice (PBS and ^{131}I -MHHD), for hematological and biochemical analysis. The hearts, livers, spleens, lungs, kidneys, thyroids, and muscles were dissected and weighed, and the organ indices were calculated. Finally, the tissues were fixed with 1% paraformaldehyde and stained with hematoxylin and eosin (H&E) to observe the histopathological changes in each organ. All animal studies were performed in accordance with the guidelines of the Animal Ethics Committee of Shanxi Medical University.

Results and discussion

Characterization of MIL-100(Fe) and MHHD

We improved the synthesis of iron-based metal organic framework MIL-100(Fe) NPs according to the method reported in reference [23]. Transmission electron microscopy (TEM) images revealed that MIL-100(Fe) exhibited a complete morphology, uniform size, and excellent dispersion (Fig. 2A). The results of X-ray photoelectron spectroscopy (XPS) full spectrum analysis revealed absorption peaks corresponding to Fe2p, C1s, and O1s in the MIL-100 (Fe) sample (Fig. 2B), indicating that the sample primarily consists of three elements: iron, carbon, and oxygen. The high-resolution spectrum of iron indicated the presence of $\text{Fe}^{2+}/\text{Fe}^{3+}$ pairs in the sample, with a loading ratio of approximately 2.38% (w/w%) for

Fe^{3+} (Fig. 2C). Then, a layer of hyaluronic acid (HA)/human serum albumin (HSA) mixture was coated on the surface of MIL-100(Fe) to obtain MIL-100(Fe)@HA-HSA (MHH), followed by loading doxorubicin (DOX) to obtain MIL-100(Fe)@HA-HSA@DOX (MHHD). TEM images (Fig. 2D) showed no significant changes in the morphology of MHHD NPs compared to MIL-100 (Fe). Comparing the surface potential and particle size changes of MIL-100(Fe) before and after encapsulating the HA/HSA mixture, the average hydrated particle size of MIL-100(Fe) increased from 146.1 ± 12.50 nm to 169.9 ± 15.28 nm (Fig. 2E). The Zeta potential decreased from -8.60 ± 0.56 mV to -30.08 ± 0.58 mV, attributable to the negatively charged carboxyl groups in HA. After loading with positively charged DOX, the Zeta potential increased to -16.66 ± 0.57 mV (Fig. S1). These results indicated the nanocarrier's successful encapsulation of HA/HSA on MIL-100 (Fe) and the loading of DOX. The UV visible absorption spectroscopy results revealed that MIL-100(Fe) and DOX exhibited characteristic absorption peaks at 213 nm and 480 nm, respectively. The absorption spectrum of MHHD displayed the characteristic peaks of MIL-100(Fe), while the absorption peak of DOX shifts from 480 nm to 490 nm. This shift was due to the DOX loading in the outer layer of the carrier HSA, further confirming the successful loading of DOX (Fig. 2F). The drug encapsulation efficiency of MHHD reached $93.28 \pm 5.45\%$, and the drug loading capacity reached $44.01 \pm 1.49\%$. There was not significant difference in the drug loading and encapsulation efficiencies compared to MIL-100(Fe)@HSA@DOX (MHD), indicating that the addition of the HA targeting molecule did not affect its drug loading capacity (Fig. S2).

Subsequently, the drug release ability of MHHD was evaluated under different pH environments. Due to the instability of MIL-100 (Fe) under acidic conditions, the release rate of DOX in acidic solution (pH=5.5) was significantly higher than that in neutral solution. GSH can reduce Fe^{3+} to Fe^{2+} , disrupting the coordination bonds within the MIL-100 framework and accelerating its degradation, thereby facilitating the release of DOX. Moreover, the thiol groups in GSH can compete with metal nodes for coordination, accelerating the framework's decomposition [29, 30]. To simulate the high GSH concentration in the tumor microenvironment, the DOX release was measured under GSH conditions. The results showed that, under the same pH conditions, the release rate of DOX in the presence of GSH was significantly increased. As the increase of GSH concentration, the release rate of DOX further elevated. At pH=5.5 and 10 mmol GSH, the cumulative release rate of DOX reached $69.93 \pm 8.02\%$ after 72 h (Fig. 2G). These findings demonstrated that MHHD can achieve controlled drug release by leveraging the tumor microenvironment. The

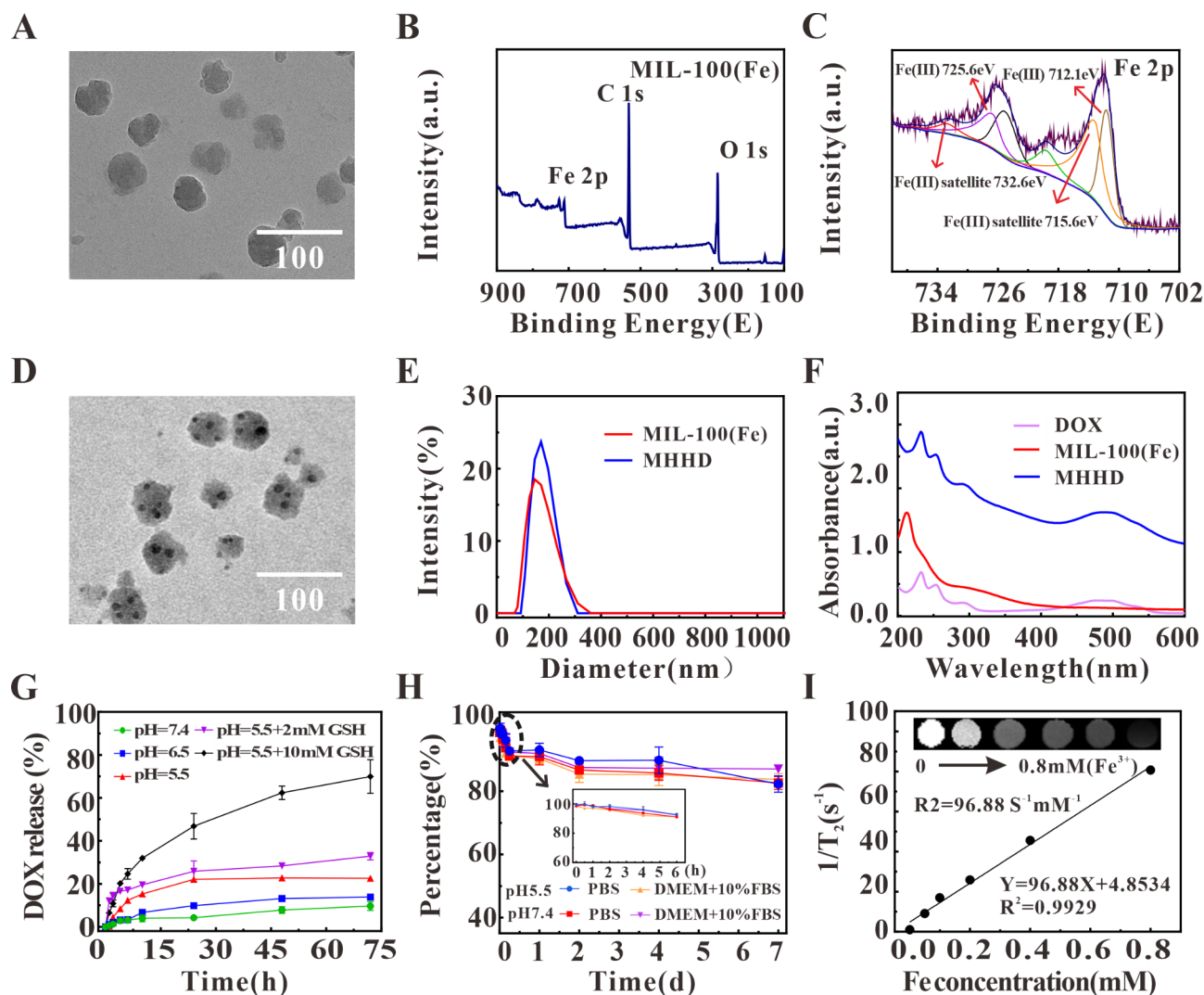


Fig. 2 The transmission electron microscopy (TEM) (A), XPS full spectrum (B) and fine spectrum of iron element (C) of MIL-100(Fe); the TEM of MHHD (D); the size distribution of MIL-100(Fe) (0.01 mg/mL) and MHHD (0.01 mg/mL) (E) and the UV-vis absorption spectra of DOX (0.015 mg/mL); MIL-100(Fe) (0.02 mg/mL), MHHD (0.04 mg/mL) (F); cumulative release rates of DOX at different conditions (G); the stability of radionuclide labeling of ^{131}I -MHHD in PBS and DMEM medium containing 10% fetal bovine serum (DMEM+10% FBS) in pH 5.5/7.4 after different time storage (H); the relationship between relaxation rate R_2 ($1/T_2$) and MHHD at different Fe^{3+} concentrations (insert: T_2 weighted MR images of MHHD at different concentrations) (I)

acid-responsive characteristics of MHHD was further investigated. TEM results confirmed that MHHD underwent significant degradation after being exposed to pH 5.5 for 24 h, showing irregular particle shapes observed. In contrast, only partial degradation was observed at pH 7.4 (Fig. S3). This suggested that MHHD may be an acid-sensitive metal-organic framework, potentially allowing for degradation and drug release in the acidic microenvironment of tumors.

Additionally, the biocompatibility of carrier is a crucial factor for their in vivo applications. Its hemolytic effect severely limited its delivery process in the body, thus, the hemolysis tests of MHH was conducted. The results showed that even at concentration of MHH 800 $\mu\text{g}/\text{mL}$, the hemolysis rate remained below 5% (Fig. S4),

indicating that the delivery carrier possessed good biocompatibility and provided potential for in vivo tumor treatment. The tyrosine-rich HSA was used to label ^{131}I onto MHHD by the chloramine-T labeling method, producing ^{131}I -MMHD. To confirm the stable labeling of ^{131}I on the carrier, the labeled carrier was washed and centrifuged, and the radioactivity of free ^{131}I in the supernatant was measured. The experimental data demonstrated that the radioactivity of the supernatant remained consistently below 2% after three consecutive centrifugation cycles. Following four rounds of centrifugation, the supernatant contained less than 0.2% (Fig. S5). This observation confirmed that the ^{131}I adsorbed on the surfaces of the ^{131}I -MHH, ^{131}I -MHD, and ^{131}I -MHHD precipitates was effectively eliminated through the

washing process. After three rounds of centrifugal washing of labeling yield of ^{131}I -MHH, ^{131}I -MHD, ^{131}I -MHHD was respectively determined to be $67.38 \pm 2.18\%$; $65.48 \pm 2.76\%$, $65.85 \pm 3.46\%$ [31]. Next, we conducted experiments to validate the radio-stability of ^{131}I -MHD and ^{131}I -MHHD at different time points under PBS conditions at pH 5.5 and pH 7.4, as well as in DMEM with 10% FBS. The results showed that the radio-stability of the non-encapsulated hyaluronic acid nanoparticle ^{131}I -MHD was 91.11% and 85.99% under acidic conditions in PBS and DMEM + 10% FBS, respectively, and 90.82% and 91.09% under neutral conditions (Fig. S6). Conversely, ^{131}I -MHHD demonstrated radio-stability of 93.05% and 90.35% under acidic conditions after 24 h, with no significant difference compared to ^{131}I -MHD ($P > 0.05$). On day 7, both ^{131}I -MHD and ^{131}I -MHHD maintained radio-stability above 82% in both acidic and neutral conditions, also showing no significant difference ($P > 0.05$) (Fig. 2H). Additionally, we also evaluated MRI capability of MHHD. As the concentrations of MHHD increased, darker MRI images were obtained. The transverse relaxivity (R_2) of MHHD was approximately $96.88 \text{ mM}^{-1}\text{s}^{-1}$ (Fig. 2I), which is comparable to that of the commercial T_2 -MR contrast agent Resovist (e.g., Fe_3O_4 NPs with $98.3 \text{ mM}^{-1}\text{s}^{-1}$), indicating MHHD's potential as a novel MRI contrast agent [32]. These excellent properties of

metal-organic frameworks form a solid foundation for further in vivo and in vitro studies.

Cellular uptake

Efficient tumor targeting is fundamental for precise delivery carriers. By modifying the surface of the carrier with targeted ligands, it can recognize and bind to receptors expressed on target cells, triggering receptor-mediated endocytosis and enhancing probe uptake. In this study, 4T1 cells, which exhibit high CD44 receptor expression, and 3T3 cells, with low CD44 receptor expression, were selected as positive and negative models for HA-targeted recognition, respectively. MHHD was co-incubated with 3T3 and 4T1 for 1, 2, and 4 h, and then analyzed using flow cytometry (Fig. 3A). Results demonstrated that intracellular fluorescence intensity increased over time. After 4 h, the fluorescence intensity of doxorubicin uptake in 3T3 cells was $87.2 \pm 2.13\%$, while it reached $98.4 \pm 1.22\%$ in 4T1 cells. At the same time point, the average fluorescence intensity in 4T1 cells was significantly higher than that in 3T3 cells ($P < 0.01$) (Fig. 3B). This indicated that MHHD uptake increased significantly over time, likely due to the overexpression of CD44 receptors on 4T1 cells, which tightly bind to HA, enhancing MHHD uptake ($P < 0.01$).

To further confirmed that CD44-positive 4T1 cells exhibit greater uptake of MHHD compared to 3T3 cells,

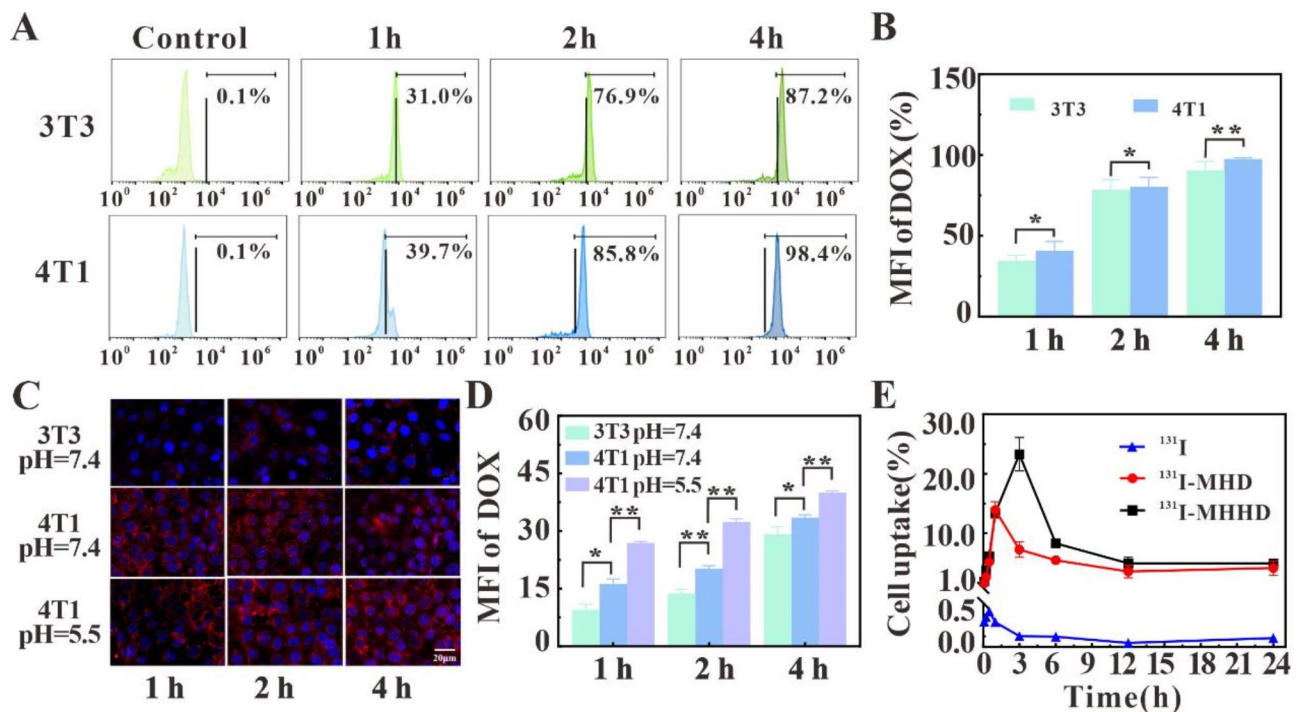


Fig. 3 Flow cytometry analysis of MHHD (4.54 $\mu\text{g}/\text{mL}$, DOX at 2 μg) NPs incubated with 3T3 and 4T1 cells at different times (A) and its quantitative analysis (B); Confocal laser scanning microscope images (C) and DOX fluorescence semi-quantitative analysis (D) of MHHD NPs (4.54 $\mu\text{g}/\text{mL}$, DOX at 2 μg) incubated with 3T3 or 4T1 cells at pH 7.4/5.5, DAPI:1 $\mu\text{g}/\text{mL}$, Scale bar = 50 μm ; the uptake of ^{131}I , ^{131}I -MHD and ^{131}I -MHHD (10 $\mu\text{Ci}/\text{mL}$) in 4T1 cells at different time using a gamma counter (E)

thereby validating the targeting capability of MHHD of HA, we conducted MHHD uptake in 3T3 and 4T1 cells was also observed using confocal microscopy under identical conditions (pH=7.4), with nuclei stained by DAPI. The results showed weak red fluorescence of DOX in 3T3 cells at pH 7.4, but significantly higher red fluorescence signals in 4T1 cells ($P < 0.01$). This difference was attributed to negative CD44 expression in 3T3 cells and overexpression in 4T1 cells (Fig. 3C). The tumor microenvironment typically has a lower pH due to enhanced glycolytic metabolism in tumor cells, leading to lactate accumulation, which coincides with increased DOX release from MHHD under acidic conditions. Therefore, to simulate the acidic conditions of the tumor microenvironment, we co-cultured 4T1 cells with nanomaterials in media at different pH levels for a specific duration to assess whether acidic conditions enhance the uptake of MHHD by 4T1 cells. The results revealed the red fluorescence intensity of DOX in 4T1 cells under acidic conditions was 1.6 times higher than that under neutral conditions after 2 h (Fig. 3D), indicating acidity enhances DOX release from MHHD. Then ^{131}I -MHHD accumulation in 4T1 cells was measured at various times using a gamma counter (Fig. 3E). Experimental results demonstrated that cellular uptake of ^{131}I -MHD and ^{131}I -MHHD was significantly higher than that of free ^{131}I , with the retention time of ^{131}I -labeled carriers in cells notably longer than that of free ^{131}I . This confirmed that nanocarriers enhanced both the uptake and retention of radionuclides in cells. The uptake of ^{131}I -MHHD was the highest, peaking at 3 h, due to the HA-targeting molecule on the carrier surface specifically recognizing the CD44 receptor on tumor cells, mediating endocytosis. These findings demonstrated that ^{131}I -MHHD specifically bound to tumor cells with high CD44 expression, improved radionuclide residence time in tumors, and achieved controlled drug release by exploiting the tumor microenvironment.

In vitro therapeutic evaluation

To advance therapeutic studies in mice, we further assessed the combined therapeutic efficacy of ^{131}I -MHHD. First, the cytotoxicity of the drug delivery carrier (MHH) alone was examined by Cell Counting Kit-8 (CCK-8) assay. The results showed that the MHH maintained cell viability above 90% for both mouse embryonic fibroblast 3T3 cells and mouse breast cancer 4T1 cells, even at a high concentration of 800 $\mu\text{g}/\text{mL}$ (Fig. 4A). This indicated that the low cytotoxicity and excellent biocompatibility of the carrier material itself. To assess the apoptosis-inducing efficacy of the ^{131}I -MHH targeted therapeutic agent, a flow cytometry-based Annexin V-FITC/propidium iodide (PI) dual staining assay was performed. The data indicated free ^{131}I group

exhibited minimal early and late apoptosis in response to cellular damage, yet demonstrated notable targeting specificity (Fig. 4B). In contrast, the ^{131}I -MHHD group showed a more pronounced trend toward early apoptosis reached 9.75% (Fig. S7), compared to ^{131}I alone, although significant late apoptosis was not observed after 24 h of incubation. To further evaluate the therapeutic impact of the radiolabeled carrier on tumor cells, the Calcein-AM (AM, green fluorescence) and PI (red fluorescence) were used to label live and dead cells respectively. The results suggested significantly higher red fluorescence intensity in the ^{131}I -MHH compared with the control and free ^{131}I groups ($p < 0.01$). Specifically, the fluorescence intensity of PI in ^{131}I -MHH was 2.75 times higher than that in the free ^{131}I group, indicating that the nanocarrier enhance the cytotoxicity of radionuclides to tumor cells (Fig. S8). These findings align with the Annexin V-FITC/PI apoptosis assay results.

Moreover, the cell viability of 3T3 and 4T1 cells after treatment with different concentrations of ^{131}I -MHHD was evaluated using CCK8 assay. It was found that at the same concentration, the survival rate of 4T1 cells was significantly lower than that of 3T3 cells. When the DOX concentration reached 5 $\mu\text{g}/\text{mL}$, the survival rate of 3T3 cells was $66.58 \pm 1.74\%$, while that of 4T1 cells was $52.98 \pm 0.96\%$ (Fig. 4C), reflecting the specific targeting ability of ^{131}I -MHHD to 4T1 cells, which enhances cytotoxicity. Then the Chou-Talalay method was employed to assess the synergistic interaction between the combined therapeutic modalities. The combination index (CI) was calculated by the Chou-Talalay method using CompuSyn version 1.0. Results indicated when fraction affected (Fa) = 0.5, $\text{CI} = 0.66 < 1$, indicating a significant synergistic effect of the combined treatment of the DOX and ^{131}I (Fig. S9). The tumor-killing efficacy of the carrier under different treatment methods was further investigated. The CCK8 assay results indicated that the free ^{131}I exhibited minimal toxicity to 4T1 cells, while the toxicity of radionuclide-labeled carriers (^{131}I -MHH, ^{131}I -MHD, ^{131}I -MHHD) increased as concentration increases. This was attributed to the carrier's ability to improve the uptake and retention time of the radionuclide in tumor cells, thereby increasing its lethality. When the radionuclide reached 7.5 $\mu\text{Ci}/\text{mL}$, the cell survival rate of the ^{131}I -MHHD group was significantly lower than that of the ^{131}I -MHD group, likely due to the CD44-targeting molecule HA in the ^{131}I -MHHD group, resulting in a more potent therapeutic effect (Fig. 4D). The cell survival rate of the ^{131}I -MHHD combined treatment group was significantly lower than that of the ^{131}I -MHH and MHHD alone treatment groups, indicating that the simultaneous combination of radionuclide therapy and chemotherapy could markedly improve the therapeutic effect. Additionally, considering the pH-responsive nature of the carrier,

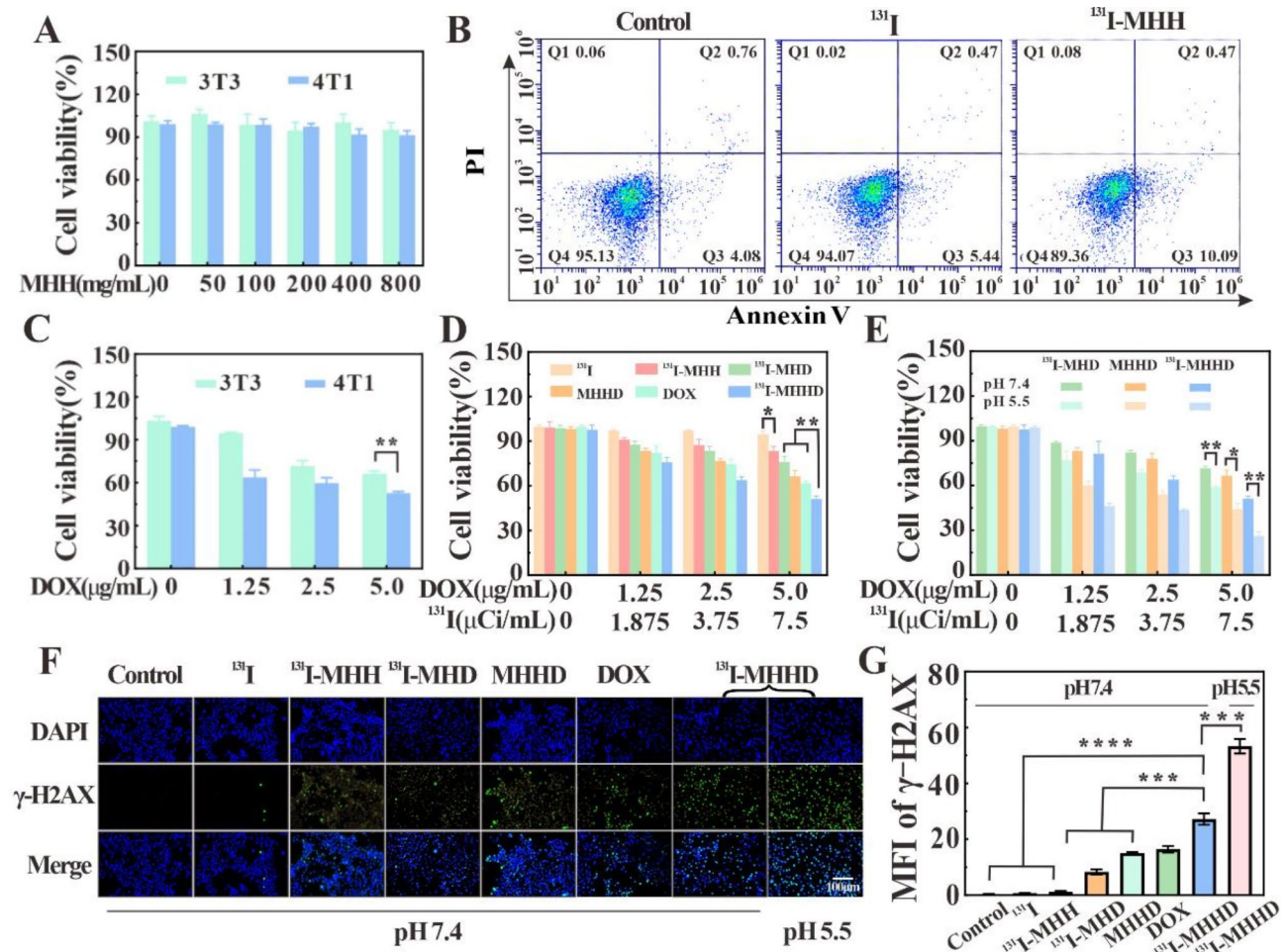


Fig. 4 Cell viabilities of 4T1/3T3 cell incubated with MHH (A); Apoptotic analysis was performed using the Annexin V-FITC/PI assay, with resolution by flow cytometry, for the following conditions: Control, ^{131}I and ^{131}I -MHH (25 μCi) (B); cell viabilities of 4T1/3T3 cell incubated with MHH (C); 4T1 cell viabilities with different concentrations of ^{131}I , ^{131}I -MHH, ^{131}I -MHD, MHH, DOX, ^{131}I -MHH (in pH 7.4) (D); 4T1 cell viabilities with different concentrations of ^{131}I -MHD, MHH, ^{131}I -MHH (in pH 7.4 and pH 5.5) (E); Graphs of γ -H2AX staining of 4T1 cells after different groups of treatments (F) and mean fluorescence intensity quantitative analysis of γ -H2AX (H). (* $p < 0.05$, ** $p < 0.01$, *** $p < 0.001$)

we also evaluated its impact on tumor cell therapy under different pH conditions, simulating an acidic tumor microenvironment. The results showed that the survival rate of 4T1 cells incubated with ^{131}I -MHD, MHH, and ^{131}I -MHH under acidic conditions (pH = 5.5) was significantly lower than that under neutral conditions (pH = 7.4) ($P < 0.05$). At a DOX concentration of 5 $\mu\text{g}/\text{mL}$ and a ^{131}I concentration of 7.5 $\mu\text{Ci}/\text{mL}$, the survival rate of 4T1 cells treated with ^{131}I -MHH was $51.27 \pm 1.92\%$. However, under acidic conditions, the survival rate of ^{131}I -MHH NPs was only $25.97 \pm 5.50\%$ ($P < 0.01$) (Fig. 4E). This difference may be attributed to the instability of the carrier under acidic conditions, leading to enhance the release of DOX and thereby improving the therapeutic effect.

To further assess DNA damage in tumor cells, the semi-quantifying γ -H2AX immunofluorescence was performed. The results showed that under neutral

conditions, the free ^{131}I group only exhibited weak green fluorescence, indicating only a small amount of DNA breaks. Additionally, the free DOX demonstrated a stronger tumor-killing effect compared to the MHH group loaded with an equivalent concentration of DOX, which was attributed to the limited release of DOX from MHH under neutral conditions. What's more, the green fluorescence intensity of the ^{131}I -MHH group was stronger than that of the free ^{131}I group, while the ^{131}I -MHH group exhibited even more intense fluorescence compared to the ^{131}I -MHD group. This observation indicated that HA encapsulated within the carrier significantly improved targeting to 4T1 cells, thereby enhancing the therapeutic effect of the probe (Fig. 4F). The green fluorescence intensity of the ^{131}I -MHH combined treatment group was notably higher than that of observed in both the radionuclide treatment group (^{131}I -MHH) and the chemotherapy treatment group

(MHHD). This finding suggested that the concurrent use of radionuclide therapy and chemotherapy achieved a superior therapeutic outcome compared to either treatment alone, consistent with the results obtained from the CCK8 method. Under acidic conditions, the fluorescence intensity of ^{131}I -MHHD was 1.87 times higher than under neutral conditions (Fig. 4G). This was attributed to the pH-responsive behavior of carrier's facilitated the synchronous release of DOX, which, in combination with radionuclides, promoted DNA damage and inhibited tumor cell proliferation. These findings confirmed the carrier's ability to respond effectively to the tumor's acidic microenvironment, thereby enhancing the combined therapeutic effects of radionuclide and chemotherapy for increased tumor cell lethality.

In vivo dual-modal imaging and in vivo distribution

MIL-100(Fe) possesses nuclear magnetic imaging capabilities, while radionuclide ^{131}I emits both β and γ rays, enabling it suitable for radiation therapy and as a tracer agent for SPECT imaging. MRI offers high spatial resolution for soft tissues, delivering accurate anatomical details and tumor mapping [33]. In contrast, SPECT imaging offers high sensitivity, quantification, and deep penetration, useful for early tumor diagnosis and in vivo drug metabolism studies [34, 35]. Integrating multiple imaging technologies offers complementary advantages and represents a promising direction in molecular imaging development. Next, MRI and SPECT imaging in 4T1 tumor-bearing mice using ^{131}I -MHHD were studied. In the experiment, ^{131}I -MHHD was administered via both tail vein and intratumoral injection, with MRI imaging performed at various time points (Fig. 5A). Following tail vein injection, a significant darkening effect was observed at the tumor site, peaking at 9 h post-injection and gradually diminishing by 24 h, with T_2 mapping values returning to pre-injection levels (Fig. 5B), indicating carrier metabolism. Additionally, intratumoral injection led to immediate probe accumulation, with a pronounced darkening effect still could be observed at the tumor site after 24 h. T_2 mapping quantitative data analysis revealed that the probe remained at the tumor site for up to 7 days (Fig. 5C).

Then, we compared the retention effects of free ^{131}I , ^{131}I -MHD, and ^{131}I -MHHD in tumor tissue by SPECT imaging. The tumor-bearing mice were randomly divided into three groups, receiving an intravenous injection of (i) ^{131}I (200 μCi , 100 μL), (ii) ^{131}I -MHD (200 μCi , 100 μL), (iii) ^{131}I -MHHD (200 μCi , 100 μL). Whole-body SPECT imaging was performed on the mice at 0, 3, 6, 9, 12, and 24 h post-injection (Fig. 5D). The results showed that ^{131}I was extensively taken up by the thyroid gland within 3 h after injection, with minimal accumulation in the organs. By 9 h post-injection, nearly all the ^{131}I was absorbed by the

thyroid gland. Conversely, the ^{131}I -MHHD group exhibited peak signal intensity at the tumor site at 9 h post-injection, with gradually decreased and minimal thyroid uptake, aligning with MRI observations. However, the non-targeted ^{131}I -MHD showed limited accumulation at the tumor site, with the majority being taken up by the thyroid. This significant difference is attributed to HA's high specificity, enhancing tumor enrichment and retention time. Following intratumoral injection of different probes, the radiolabeled carrier largely prolonged retention at the tumor site, with minimal uptake by the thyroid after 24 h, unlike free ^{131}I (Fig. S10). This may be due to gradual degradation of the carrier in the tumor microenvironment, releasing small amounts of ^{131}I absorbed by the thyroid.

Subsequently, analysis of probe biodistribution in various organs by γ -counter detection, revealed that free ^{131}I primarily accumulated in the liver, spleen, and lungs, with negligible tumor localization, and was rapidly metabolized within 6 h (Fig. 5E). In the ^{131}I -MHHD group, the probe initially distributed in the liver, spleen, lungs, and kidneys after injection, gradually being cleared over time (Fig. 5F). However, signals intensity increased at tumor site, peaking at 9 h with significant differences compared to other time points ($p < 0.01$) (Fig. S11). Results confirmed that the delivery carrier effectively retained ^{131}I at the tumor site for extended periods, reducing radiotoxicity and enabling accurate tumor diagnosis and localization via MRI /SPECT imaging.

In vivo evaluation of synchronous therapy

To assess the therapeutic effects in vivo, different probes were tested on 4T1 tumor-bearing mice, which were randomly divided into six groups ($n = 3$ per group): (i) PBS (Control), (ii) Free- ^{131}I , (iii) Free-DOX, (iv) ^{131}I -MHD, (v) MHHD and (vi) ^{131}I -MHHD. After intratumorally injected of PBS or different probes, the mice were monitored for body weight and tumor volume every two days for 30 days post-treatment. Tumors were collected on day 30 for histopathological examination and immunofluorescence staining. (Fig. 6A). Results showed that weight changes across all groups were comparable to the control, indicating no significant toxicity of the carrier (Fig. 6B). During treatment period, tumor size progressively increased in the PBS, Free- ^{131}I , Free-DOX, and ^{131}I -MHD groups (Fig. 6C). Notably, the tumor inhibition rate of the ^{131}I -MHD group was significantly lower than that of the ^{131}I -MHHD group ($P < 0.001$), which can be attributed to reduced accumulation at the tumor site due to the lack of targeted protein HA and the premature drug release during its transit through the bloodstream prior to reaching the tumor, thereby diminishing therapeutic effects. In contrast, tumor growth in the MHHD group was significantly less than that in the ^{131}I -MHD, DOX, and control

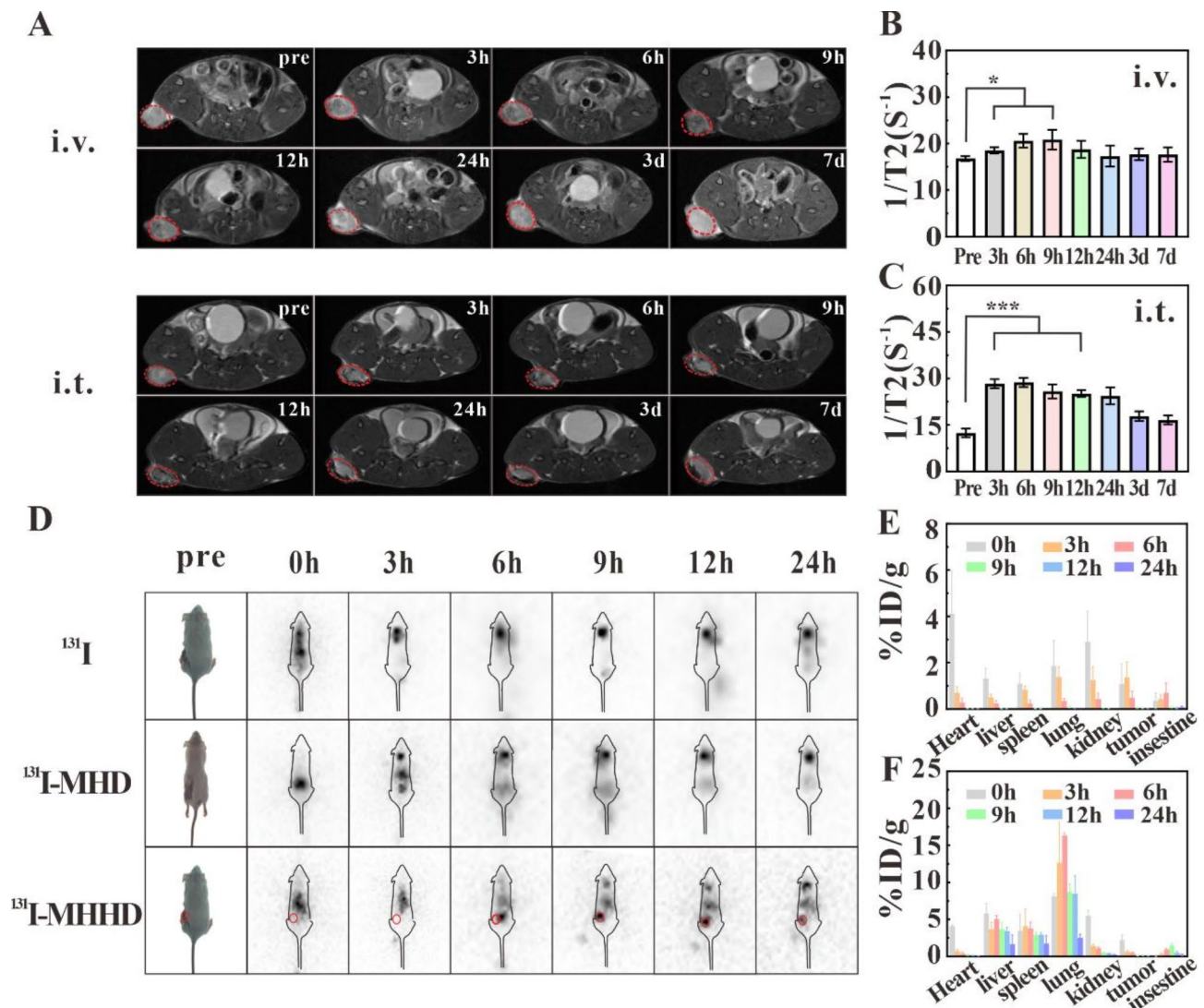


Fig. 5 T_2 -weighted MR imaging of tumor-bearing mice at various time points after intravenous and intratumoral injection of ^{131}I -MHHD (A), along with corresponding average relaxation rate R_2 ($1/T_2$) of the tumor site (B, C), with tumors circled in red. SPECT images of 4T1 tumor-bearing mice at different time points after intravenous injection of ^{131}I , ^{131}I -MHD, or ^{131}I -MHHD (D), and distribution profiles of ^{131}I (E) and ^{131}I -MHHD (F) in major organs at various time points. $n=3$, * $P<0.05$, ** $P<0.01$, *** $P<0.001$

groups, likely because MHHD's HA surface facilitated targeted drug delivery and released DOX by the tumor's acidic and high-GSH microenvironment, inhibiting growth. However, tumor growth in the ^{131}I -MHHD combination group was significantly lower than that in the MHHD group, demonstrating the enhanced inhibitory effect from the simultaneous combination of radionuclides therapy and chemotherapy (Fig. 6D).

To further investigate the antitumor effects of different probes, tumor sections from various treatments were collected for histopathological and immunofluorescence analysis. As illustrated in Fig. 6E, the control, ^{131}I , and DOX groups showed minimal tumor damage, while the ^{131}I -MHD group exhibited slight apoptosis. Tumor sections from the MHHD and ^{131}I -MMHD groups displayed

increased TUNEL green fluorescence and H&E staining revealed typical apoptotic features, such as condensed and deeply stained nuclei, with the most pronounced in the ^{131}I -MMHD group. These findings confirmed that ^{131}I -MMHD effectively targeted tumor sites, utilizing the tumor microenvironment for enhanced the co-treatment of radionuclide and chemotherapy, significantly improving tumor inhibition.

In vivo safety evaluation

Safety assessment of nanomaterials is a crucial parameter to advance clinical applications. Therefore, the in vivo biosafety of ^{131}I -MHHD was studied by analyzing blood biochemical and routine parameters in treated mice. Compared to the PBS control group, there were

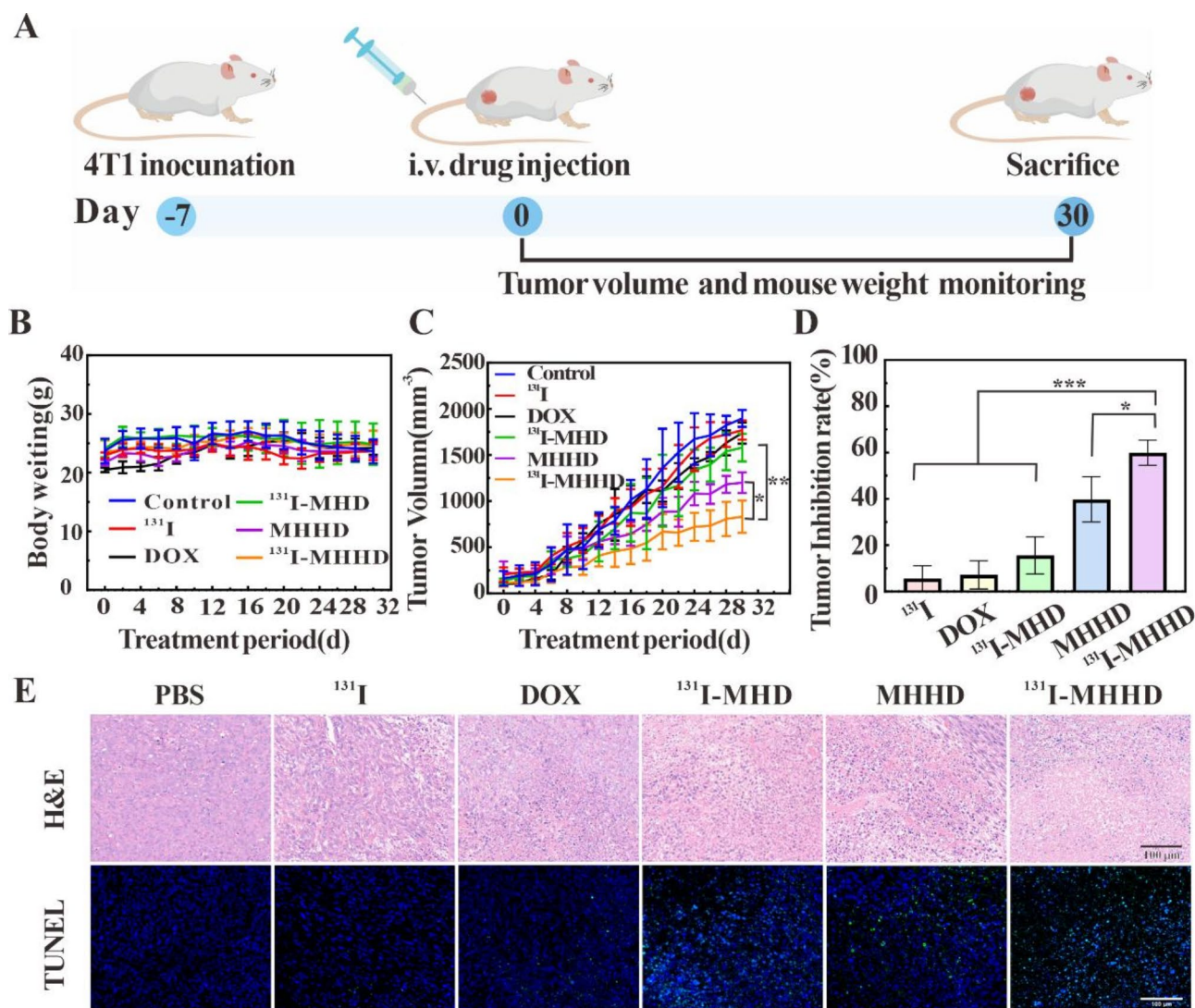


Fig. 6 Schematic illustration of treatment 4T1 tumor bearing mouse route (A); after treatment with different carriers (Control, ¹³¹I, DOX, ¹³¹I-MHD, MHHD and ¹³¹I-MHHD); body weight change curves (B); tumor volumes size change curves after treatment with different carriers (C); tumor inhibition rate (D); TUNEL and H&E stained sections of tumors after treatment with different carriers (E). $n=3$, $*p<0.05$, $**p<0.01$, $***p<0.001$

no significant differences in red blood cell count (RBC), platelet

count (PLT), hemoglobin (HGB), hematocrit (HCT), mean corpuscular hemoglobin (MCH), and mean corpuscular hemoglobin concentration (MCHC) in the treated mice ($P>0.05$) (Fig. 7A), indicating good blood safety. Serum alanine aminotransferase (ALT) and aspartate aminotransferase (AST) serve as key markers for liver injury, while blood urea nitrogen (BUN) and creatinine (CREA) are critical for assessing renal function [36]. There was no significant difference in ALT, AST, BUN and CREA levels in serum collected after treatment compared to the PBS group ($P>0.05$), suggesting that tail vein injection did not cause liver or kidney damage. Major organs, including heart, liver, spleen, lung, and kidney, were harvested for organ index analysis and

H&E staining. Both the experimental and control groups showed normal organ indexes with no significant differences (Fig. 7B), and H&E staining revealed no pathological changes (Fig. 7C). This indicated that ¹³¹I-MHHD treatment did not cause side effects, demonstrating good biological safety. Additionally, considering the high iodine uptake of the thyroid gland, the probe was further tested for its effect on the thyroid gland, and there were also no significant pathological abnormalities (Fig. S12), suggesting ¹³¹I-MHHD remained relatively stable and held promise for clinical application.

Conclusions

In summary, we have successfully constructed a new biocompatible iron-based metal-organic framework as a drug delivery carrier that responds to the tumor

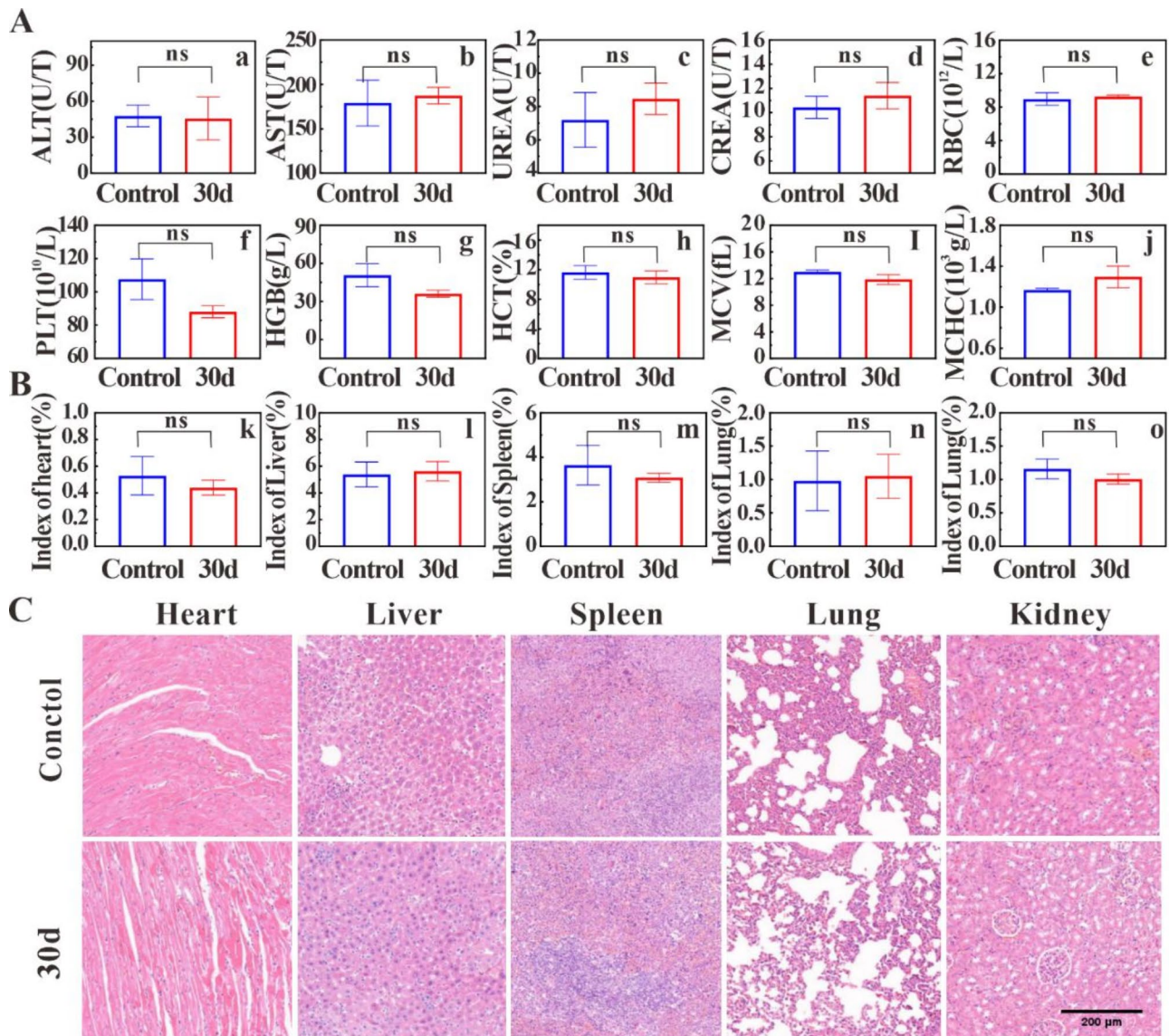


Fig. 7 Changes in Alanine aminotransferase (ALT), aspartate aminotransferase (AST), blood urea, creatinine (CREA), red blood cell count (RBC), platelet count (PLT), hemoglobin (HGB), hematocrit (HCT), mean corpuscular hemoglobin (MCH), mean corpuscular hemoglobin concentration (MCHC) (A), and indexes of the various organs were observed 30 d after PBS and ^{131}I -MHHD injection in tumor-bearing mice (B), ($n=3$); hematoxylin-eosin (H&E) stained sections of various (C)

microenvironment. This innovative carrier can load and precisely deliver both radionuclide and anticancer drugs, enabling the synchronized combination therapy of radionuclide and chemotherapy. The *in vitro* and *in vivo* experiments demonstrated that the encapsulation of hyaluronic acid allowed for targeted delivery to tumor cells overexpressing CD44 receptor. Utilizing the tumor microenvironment, the carrier enhanced the release of doxorubicin at the tumor site, thereby improving the efficacy of both radionuclide therapy and chemotherapy. This approach provides a precise and synchronized strategy, leading to enhanced therapeutic outcomes. Additionally, the carrier allowed for real-time monitoring of

its distribution within the body and enables tumor diagnosis under MRI/SPECT dual-modal imaging. Therefore, this delivery carrier held significant diagnostic and therapeutic potential for image-guided radio-chemotherapy of solid tumors, presenting a promising strategy for clinical combined radio-chemotherapy in cancer treatment.

Supplementary Information

The online version contains supplementary material available at <https://doi.org/10.1186/s12951-025-03364-4>.

Supplementary Material 1

Acknowledgements

The authors thank the Collaborative Innovation Center for Molecular Imaging and the First Hospital of Shanxi Medical University for their support of MRI and SPECT imaging.

Author contributions

Jie An and Qin Zhou designed the research, performed main analysis and drafted the manuscript. Kaile Chu and Siyuan Chen helped for cell experiments. Chenliang Niu, Min Li, Junping Lv and Weiming Zhang helped for animal experiments. Jie Gao and Zhang Di were in charge of biochemical analysis of blood. Jianbo Cao and Zhifang Wu guided MRI/SPECT imaging. Sijin Li and Hua Wei reviewed and improved it. All authors read and approved the final manuscript.

Funding

This work was financially supported by the National Natural Science Foundation of China (Grant No. 82102103, U22A6008, 82402424 and 82027804), Natural Science Foundation for Young Scientists of Shanxi Province (No. 20210302124175, 202303021212137, 202403021222232), Shanxi Provincial Department of Education (No. 20230243, 2024SJ185) and Shanxi Provincial Health Commission (No. 2024050).

Data availability

No datasets were generated or analysed during the current study.

Declarations

Ethics approval and consent to participate

All Institutional and National Guidelines for the care and use of animals were followed. All the animal experiments were approved by the Animal Ethics Committee of Shanxi Medical University.

Consent for publication

All authors consent for publication.

Competing interests

The authors declare no competing interests.

Declaration of competing interest

The authors declare that they have no known competing financial interests or personal relationships that could have appeared to influence the work reported in this paper.

Author details

¹Department of Nuclear Medicine, The First Hospital of Shanxi Medical University, Shanxi Medical University, Taiyuan 030001, Shanxi, P. R. China

²Shanxi Key Laboratory of Molecular Imaging, Shanxi Medical University, Taiyuan 030001, Shanxi, P. R. China

³Collaborative Innovation Center for Molecular Imaging of Precision Medicine, Shanxi Medical University, Taiyuan 030001, Shanxi, P. R. China

⁴Academy of Medical Sciences, Shanxi Medical University, Taiyuan 030001, Shanxi Province, P. R. China

⁵CAEA Center of Excellence on Nuclear Technology Applications for Nonclinical Evaluation for Radiopharmaceutical, Shanxi Key Laboratory of Drug Toxicology and Preclinical Studies for Radiopharmaceutical, Shanxi Province 030006 Taiyuan, P. R. China

Received: 20 December 2024 / Accepted: 1 April 2025

Published online: 15 April 2025

References

1. Peltek OO, Karpov TE, Rogova A, et al. Development of Nanocarrier-Based radionuclide and photothermal therapy in combination with chemotherapy in melanoma cancer treatment. *ACS Appl Mater Interfaces*. 2023;15(10):13460–71. <https://doi.org/10.1021/acsami.2c20619>.
2. An J, He XY, Ma HZ, et al. Radionuclide labeled nanocarrier for imaging guided combined radionuclide, sonodynamic, and photothermal therapy of pancreatic tumours. *J Colloid Interface Sci*. 2023;642:789–99. <https://doi.org/10.1016/j.jcis.2023.03.111>.
3. Llop J, Lammers T. Nanoparticles for cancer diagnosis, radionuclide therapy and theranostics. *ACS Nano*. 2021;15(11):16974–81. <https://doi.org/10.1021/acsnano.1c09139>.
4. Wang C, Li N, Li Y, et al. Engineering a HEK-293T exosome-based delivery platform for efficient tumor-targeting chemotherapy/internal irradiation combination therapy. *J Nanobiotechnol*. 2022;20(1):247. <https://doi.org/10.1186/s12951-022-01462-1>.
5. Zhang Y, Wang GL, Li Q, et al. Acidity-Activated charge conversion of ¹⁷⁷Lu-Labeled nanoagent for the enhanced photodynamic radionuclide therapy of cancer. *ACS Appl Mater Interfaces*. 2022;14(3):3875–84. <https://doi.org/10.1021/acsami.1c21860>.
6. Karpov T, Postovalova A, Akhmetova D, et al. Universal Chelator-Free radio-labeling of organic and Inorganic-Based nanocarriers with diagnostic and therapeutic isotopes for internal radiotherapy. *Chem Mat*. 2022;13. <https://doi.org/10.1021/acs.chemmater.2c01507>.
7. Li SJ, Wang Y, Wang XR, et al. Macrocyclic-Albumin conjugates for precise delivery of radionuclides and anticancer drugs to tumors. *ACS Nano*. 2023;17(22):22399–409. <https://doi.org/10.1021/acsnano.3c04718>.
8. Lihui X, Chenjun B, Zhao J, et al. Radiation-targeted immunotherapy: A new perspective in cancer radiotherapy. *Cytokine Growth Factor Rev*. 2024;75:1–11. <https://doi.org/10.1016/j.cytogfr.2023.11.003>.
9. Morgan KA, Wichmann CW, Osellame LD, et al. Tumor targeted alpha particle therapy with an actinium-225 labelled antibody for carbonic anhydrase IX. *Chem Sci*. 2024;15(9):3372–81. <https://doi.org/10.1039/d3sc06365h>.
10. Garrido G, Schrand B, Rabasa A, et al. Tumor-targeted Silencing of the peptide transporter TAP induces potent antitumor immunity. *Nat Commun*. 2019;10(1):3773. <https://doi.org/10.1038/s41467-019-11728-2>.
11. Kanai Y. Amino acid transporter LAT1 (SLC7A5) as a molecular target for cancer diagnosis and therapeutics. *Pharmacol Ther*. 2022;230:107964. <https://doi.org/10.1016/j.pharmthera.2021.107964>.
12. Liu X, Olszewski K, Zhang Y, et al. Cystine transporter regulation of Pentose phosphate pathway dependency and disulfide stress exposes a targetable metabolic vulnerability in cancer. *Nat Cell Biol*. 2020;22(4):476–86. <https://doi.org/10.1038/s41556-020-0496-x>.
13. Kang Y, Sun W, Li S, et al. Oligo Hyaluronan-Coated silica/hydroxyapatite degradable nanoparticles for targeted cancer treatment. *Adv Sci (Weinh)*. 2019;6(13):1900716. <https://doi.org/10.1002/adv.201900716>.
14. Zeng LJ, Ding SS, Cao YH, et al. A MOF-Based potent ferroptosis inducer for enhanced radiotherapy of triple negative breast cancer. *ACS Nano*. 2023;17(14):13195–210. <https://doi.org/10.1021/acsnano.3c00048>.
15. Ilyas S, Szymura SEMS. Validation of Dual-Action Chemo-Radio-Labeled nanocarriers with high efficacy against Triple-Negative breast cancer. *ACS Appl Mater Interfaces*. 2023;15(42):48963–77. <https://doi.org/10.1021/acsami.3c10579>.
16. Nae-Won K, Voradanu V, Duy-Thuc N, et al. Bone tumor-homing nanotherapeutics for prolonged retention in tumor microenvironment and facilitated apoptotic process via mevalonate pathway Inhibition. *Mater Today Bio*. 2023;19:100591. <https://doi.org/10.1016/j.mtbio.2023.100591>.
17. Zhou M, Wang X, Xia J, et al. A Mansonone derivative coupled with monoclonal antibody 4D5-Modified Chitosan inhibit AKR1C3 to treat Castration-Resistant prostate cancer. *Int J Nanomed*. 2020;15:3087–98. <https://doi.org/10.2147/IJN.S241324>.
18. Xiao Y, Zhang T, Ma X, et al. Microenvironment-Responsive Prodrug-Induced pyroptosis boosts cancer immunotherapy. *Adv Sci (Weinh)*. 2021;8(24):e2101840. <https://doi.org/10.1002/adv.202101840>.
19. Pei P, Shen WH, Zhou HL, et al. Radionuclide labeled gold nanoclusters boost effective anti-tumor immunity for augmented radio-immunotherapy of cancer. *Nano Today*. 2021;38:13. <https://doi.org/10.1016/j.nantod.2021.101144>.
20. Wei D, Sun Y, Zhu H, Fu Q. Stimuli-Responsive Polymer-Based nanosystems for cancer theranostics. *ACS Nano*. 2023;17(23):23223–61. <https://doi.org/10.1021/acsnano.3c06019>.
21. Zhang Y, Qi L. MOF-derived nanoarrays as advanced electrocatalysts for water splitting. *Nanoscale*. 2022;14(34):12196–218. <https://doi.org/10.1039/d2nr03411e>.
22. Lim JYC, Goh L, Otake KI, Goh SS, Loh XJ, Kitagawa S. Biomedically-relevant metal organic framework-hydrogel composites. *Biomater Sci*. 2023;11(8):2661–77. <https://doi.org/10.1039/d2bm01906j>.
23. Cai W, Gao H, Chu C, et al. Engineering phototheranostic nanoscale Metal–Organic frameworks for multimodal Imaging-Guided cancer therapy. *ACS Appl Mater Interfaces*. 2017;9(3):2040–51. <https://doi.org/10.1021/acsami.6b11579>.

24. Abuçafy MP, Frem RCG, Polinario G, et al. MIL-100(Fe) Sub-Micrometric capsules as a dual drug delivery system. *Int J Mol Sci.* 2022;23(14). <https://doi.org/10.3390/ijms23147670>.
25. Hoppmann S, Qi S, Miao Z, 177Lu-DO3, A-HSA-Z et al. EGFR:1907: characterization as a potential radiopharmaceutical for radionuclide therapy of EGFR-expressing head and neck carcinomas, *J Biol Inorg Chem.* 2012;17(5):709–718. <https://doi.org/10.1007/s00775-012-0890-3>
26. Wang S, Zhou X, Zeng Z, et al. Atovaquone-HSA nano-drugs enhance the efficacy of PD-1 Blockade immunotherapy by alleviating hypoxic tumor microenvironment. *J Nanobiotechnol.* 2021;19(1):302. <https://doi.org/10.1186/s12951-021-01034-9>.
27. Chen J, Liang C, Song X, et al. Hybrid protein Nano-Reactors enable simultaneous increments of tumor oxygenation and Iodine-131 delivery for enhanced radionuclide therapy. *Small.* 2019;15(46):e1903628. <https://doi.org/10.1002/smll.201903628>.
28. Li Y, Liu L, Shang H, et al. Self-Assembling anchorage of hyaluronic acid on the nanoparticle surface confers superiority of triple negative breast cancer treatment. *Pharmaceutics.* 2022;14(11). <https://doi.org/10.3390/pharmaceutics14112461>.
29. Wan X, Zhong H, Pan W, et al. Programmed release of Dihydroartemisinin for synergistic cancer therapy using a CaCO(3) mineralized Metal-Organic framework. *Angew Chem Int Ed Engl.* 2019;58(40):14134–9. <https://doi.org/10.1002/anie.201907388>.
30. Chen T, Han G, Li X. Platinum-copper alloy nanoparticles armored with chloride ion transporter to promote electro-driven tumor Inhibition. *Bioact Mater.* 2022;12:143–52. <https://doi.org/10.1016/j.bioactmat.2021.10.012>.
31. Wu S, Ma K, Qiao WL, et al. Anti-metastatic effect of 131I-labeled *Buthus martensii* Karsch chlorotoxin in gliomas. *Int J Mol Med.* 2018;42(6):3386–94. <https://doi.org/10.3892/ijmm.2018.3905>.
32. Wang YX. Superparamagnetic iron oxide based MRI contrast agents: current status of clinical application. *Quant Imaging Med Surg.* 2011;1(1):35–40. <https://doi.org/10.3978/j.issn.2223-4292.2011.08.03>.
33. Gao D, Shi Y, Ni J, et al. NIR/MRI-Guided Oxygen-Independent Carrier-Free Anti-Tumor Nano-Theranostics. *Small.* 2022;18(36):e2106000. <https://doi.org/10.1002/smll.202106000>.
34. Bernsen MR, Vaissier PE, Van Hohen R, Booi J, Beekman FJ, de Jong M. The role of preclinical SPECT in oncological and neurological research in combination with either CT or MRI. *Eur J Nucl Med Mol Imaging.* 2014;41(1):S36–49. <https://doi.org/10.1007/s00259-013-2685-3>.
35. Ritt P. Recent developments in SPECT/CT. *Semin Nucl Med.* 2022;52(3):276–85. <https://doi.org/10.1053/j.semnuclmed.2022.01.004>.
36. Zhang N, Shu G, Shen L, et al. Biomimetic mesoporous polydopamine nanoparticles for MRI-guided photothermal-enhanced synergistic cascade chemodynamic cancer therapy. *Nano Res.* 2022;15(6):5262–72. <https://doi.org/10.1007/s12274-022-4165-1>.

Publisher's note

Springer Nature remains neutral with regard to jurisdictional claims in published maps and institutional affiliations.